Radioactivity distribution at MAFF

F. Nebel[1,2,a], J. Szerypo[2,3], E. Zech[1,2], T. Faestermann[1,2], R. Groetzschel[4], M. Groß[2,3], D. Habs[2,3], R. Krücken[1,2], P. Maier-Komor[1,2], P.G. Thirolf[2,3], and A. Yakushev[5]

[1] TU München, Physik Department E12, 85748 Garching, Germany
[2] Maier-Leibnitz-Labor für Kern- und Teilchenphysik, 85748 Garching, Germany
[3] LMU München, Department für Physik, 85748 Garching, Germany
[4] Forschungszentrum Rossendorf, 01314 Dresden, Germany
[5] TU München, Department für Radiochemie, 85748 Garching, Germany

Abstract. A detailed account on the distribution of radioactive nuclei in the vacuum system of the planned Munich Accelerator for Fission Fragments (MAFF) located at the FRM-II research reactor is presented. Tools used for the simulation of spacial and temporal distribution of radionuclides are explained. The latter allows for a detailed activity budget as well as estimates for the mass-separated ion yields at MAFF. Additionally, a concept to reduce the activity release from the MAFF slit system due to surface sputtering is presented. It is shown, that the use of low-density carbon foam, as a surface coating, reduces sputtering by orders of magnitude.

PACS. 28.41.Ak Theory, design, and computerized simulation – 28.52.Fa Materials – 28.52.Nh Safety – 29.27.Eg Beam handling; beam transport

1 Layout of MAFF

The Munich Accelerator for Fission Fragments (MAFF) [1] is a reactor-based Radioactive Ion Beam (RIB) facility, which is being planned at the high-flux reactor FRM II by the groups for nuclear physics at the Ludwig-Maximilians-University, the Technical University Munich and the Maier-Leibnitz-Laboratory (MLL) in close collaboration with the FRM II.

As a RIB facility MAFF faces the additional challenge of handling activities of 10^{14} Bq, that requires a well-planned safety concept to reduce production and release of radionuclides to an absolute minimum. For the development of a reasonable safety concept it is imperative to know the distribution of radionuclides within the facility. Neutral volatile radionuclides spreading from the ion source require special attention because of their ability to spread far from the source, while ionized particles contained in the ion beam are intentionally transported to areas hardly accessible by neutral radionuclides. Therefore, the behavior of both neutral and ionized radionuclides is addressed in this paper.

The construction of MAFF will be separated in two phases. During MAFF-I the project is focusing on low-energy experiments in the experimental hall of the

FRM II. In the second stage, MAFF-II, the project is extended to an additional building where a high-resolution mass separator and the post-accelerator are placed together with various experimental stations for additional low- and high-energy physics.

MAFF will be installed at the through-going beam tube SR-6 of the FRM II as shown in fig. 1. The ion source, loaded with a maximum of 2 g ^{235}U (1.2 g are sufficient to achieve $1 \cdot 10^{14}$ fissions/s, total neutron flux at target position $\Phi_{tot} = 9.7 \cdot 10^{13}$ n cm^{-2} s^{-1}, thermalization level 84%) as a fission target, is inserted from the B-side, while the beam is extracted in the opposite direction (A-side). Both, ion optics and source are mounted on removable separate trolleys. In-pile vacuum is maintained by applying cryopumping techniques provided by the cryopanels.

The vacuum system is split into three major sections. The first section contains the in-pile components and extends from the injection side (B-side) sealing valve to the H-stack on the extraction side (A-side) in front of the multi-purpose unit (MPU). The H-stack is a combination of three similar gate valves with one of them having a permanent central opening of about 2 cm for the ion beam. Under normal conditions only this valve is "closed". The second section extends to a series of fast shutters just after the MPU. The MPU serves as a pumping station, contains the retractable electrostatic 31.5° deflector and functions

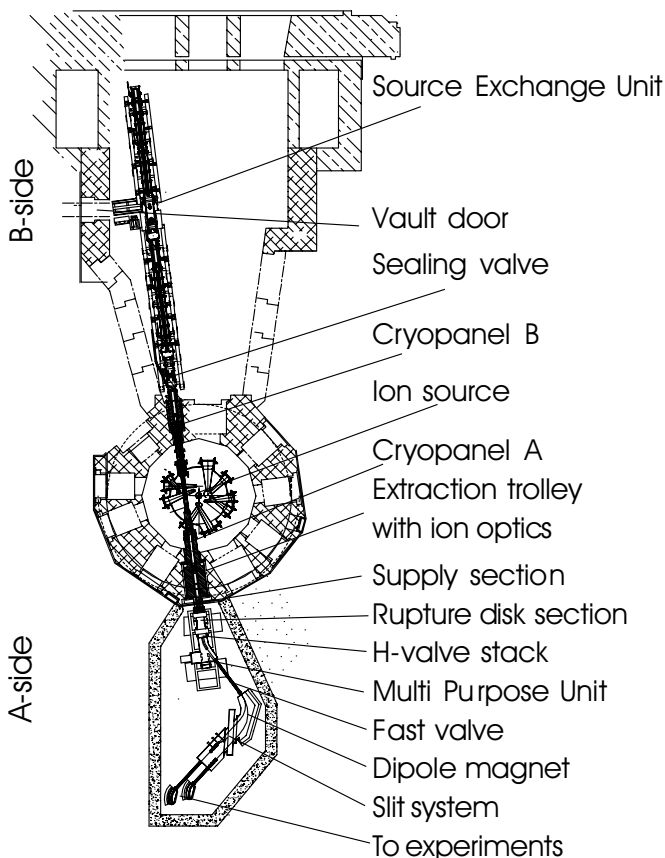[a] e-mail: florian.nebel@physik.tu-muenchen.de

Fig. 1. Brief overview of the MAFF-I facility. In the center of the figure the reactor fuel element, surrounded by the various neutron guides can be seen. The ion source is inserted in the reactor from the B-side, ions are extracted from the A-side and electrostatically guided to the experiments after mass pre-separation.

Fig. 2. Schematic drawing of the slit system. Inspired by a curtain, the slit position can be variably adjusted. A steering capability is added by applying voltage onto the slits.

as a docking station if the lens trolley needs to be exchanged. The third section reaches beyond the magnet to the beginning of the experiment vacuum.

Two electrostatic triplets and a doublet are used to extract the beam and transport the ions towards the Mattauch-Herzog–type mass pre-separator [2] with a moderate resolving power $\frac{m}{\Delta m} \approx 200$. Unwanted ions are stopped at the slit system in the focal plane of the dipole magnet. Finally, two beams, one from each mass peak of the fission fragment distribution, are guided towards low- and high-energy experiments.

The slit system behind the mass pre-separator is the beam stop for all ionized fission fragments aside from those two masses that are selected for further transport towards the experiments. The slit system is the third largest deposit of activity within the beam line, next to the cryopanels and the ion source. Due to the restricted space in this area it is planned to contain these radionuclides on the slits in order to minimize the volume that needs to be surrounded by shielding material. A schematic drawing of the slit system is given in fig. 2. The structure requires adjustable slits, to vary the mass ratio between the two selected mass peaks. Since the subsequent ion optics are
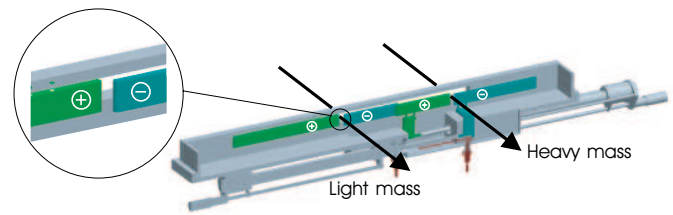
fixed in place an additional steering capability is required. This is implemented into the slit system by designing the slits as electrostatic deflectors, *e.g.* by using a curtain-like structure as shown in fig. 2.

2 Investigative tools

For complementarity and cross-reference two simulations have been carried out. For time-independent simulations the commercial programm MOVAK3D [3] was used [4]. Originally developed for conductance simulations of vacuum systems with cryopumps it could be used for MAFF as well. It gives a reasonably accurate estimate of the distribution of the radionuclides in the system, but is not capable of simulating radioactive decay. In order to obtain information on the decay and in particular on the time-dependent evolution of the activities in the system, a custom code has been developed [5]. This code includes a time-dependent Monte Carlo procedure for release and ionization probabilities in the source, radioactive decay of the fission products as well as the element-dependent sticking and release probabilities on cold and warm surfaces. In addition, external time-dependent actions like switching of valves, removing the source from the irradiation position, and warm-up of the cryopanels are included in the code.

Finally, analytical calculations based on the law of radioactive decay have been used for further calculations.

2.1 Time-independent simulations

Time-independent simulations have been performed with MOVAK3D. The code calculates trajectories of atoms independent of the element in an arbitrary geometry. For the geometry used in the code some simplifications have been made to obtain a cylindrically symmetric layout. All cold surfaces, cryopumps and panels are assumed to be fully absorbing, while all other surfaces reflect gaseous particles. During this reflection, particles hitting a wall are re-emitted following a cosine distribution. Trajectory calculations take very long and the total computation time invested sums to more than half a year. The simulated volume extends from the vacuum seal on the source side to some point several meters behind the separator. This point is referred to as the end absorber. It is a virtual surface

Table 1. Fraction of particles absorbed at the cryopumps C3–C7, at the two cryopanels and reaching the end absorber.

C3	C4	C5	C6	C7	Panel A	Panel B	End absorber
$1 \cdot 10^{-4}$	$8 \cdot 10^{-6}$	$6 \cdot 10^{-5}$	$4 \cdot 10^{-6}$	$< 4 \cdot 10^{-9}$	0.4	0.6	$9 \cdot 10^{-8}$
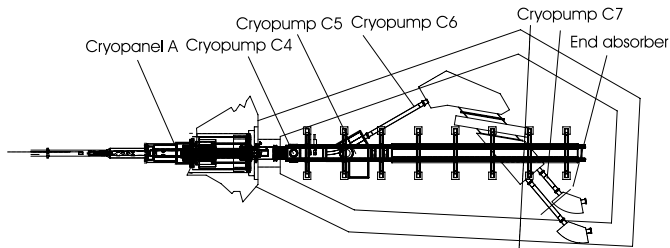
Fig. 3. Extraction side cryosurfaces. Volatile radionuclides can only be absorbed on cryosurfaces. These are provided by the cryopanels and cryopumps labelled in the drawing. The end absorber is an arbitrary surface absorbing all particles which would leave the simulated volume.

Fig. 4. Schematics of the MAFF B-side with indicated source side cryosurfaces. Only one cryopump is active at the source side, since the beam line is closed by a valve soon after cryopump C3.

that counts the amount of particles leaving the simulated volume.

One of the approximations used is that of a straight beam line. While in reality particles coming directly from the source are stopped in the multi-purpose unit (MPU), they would hit the end absorber in the simulation due to the approximation mentioned above. To prevent this, a beam sized stopper is placed in the beam tube at the position of the MPU to block the straight path. It has been made sure that the conductance with and without the stopper is equal. The vacuum chamber of the magnet is replaced by a cone giving credit to the growing volume. The cryopumps' absorbing surfaces are simulated as cylindrical, with an area equal to the cross-section of the cryopump inlet flange.

Stable particles are generated in the source, on a ring-shaped surface and are emitted following a cosine distribution. All memory of the generation process is lost due to the occurrence of many wall interactions before the particles finally emerge from the ion source. The code is not able to consider ionization, therefore ionized particles are not accounted for.

It is clear from the input to this simulation that most of the particles will be trapped on either one of the cryopanels or on one of the cryopumps. An overview of the position of cryosurfaces on the extraction side (A-side) is given in fig. 3.

Cryopumps C4 to C7 are placed on the A-side as can be seen in fig. 3. The cryopump C3 is located on the source side (B-side), just before the valve, as shown in fig. 4.

In a first calculation more than 10^6 events were simulated. None of the particles arrived at the end absorber, 99.98% of the particles were absorbed by the cryopanels. To obtain the fraction of particles arriving at the end absorber, a second simulation was performed with deactivated cryopanels in order to allow more particles to reach the end absorber. From this simulation, the fraction of particles reaching the end absorber is calculated to be
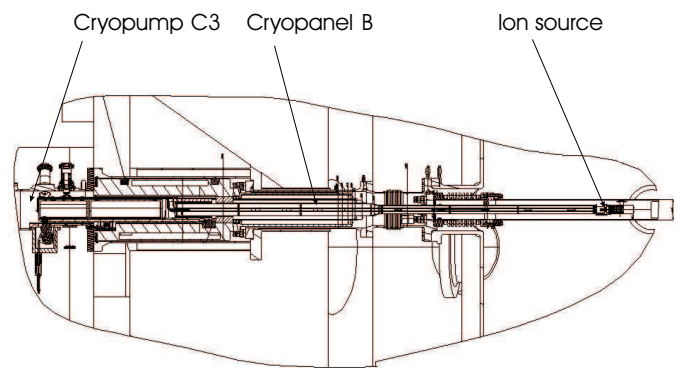
$9 \cdot 10^{-8}$. A complete summary of the results is given in table 1.

At first glance it is unexpected that the cryopump C5 collects more atoms than the cryopump C4. However, this is easily explained by the direct neutral current coming from the source hitting the stopper plate placed in the MPU directly in front of the cryopump C5 as described above. Also not intuitively clear is why the cryopump C7 collects less atoms than the end absorber. This is due to the poorer conductance to the cryopump C7 compared to the end absorber, which arises from the fact that the cryosurface is not placed immediately at the beam line but at some distance away from it.

For additional insights simulations with a cryopanel sticking coefficient (the probability of a particle sticking to a given surface) equal to 0.2 only (full absorbtion corresponds to 1.0) have been performed. It was found that the efficiency of the panels does not strongly depend on the sticking coefficient because every re-emitted particle has a very high chance of hitting the cold surface again, so that multiple hits are very common. This exponentially decreases the chance of a particle escaping the cryopanel.

2.2 Time-dependent simulations

The time-independent simulations have shown how the radioactive atoms will distribute within the system. In order to provide insights into the time-dependent and isotope specific activity distribution in the system some kind of time-dependent calculation is needed. The most accurate approach would certainly be a 3D trajectory calculation, as MOVAK3D, with added time dependence. However, no suitable program was available and the computation time for a 4-dimensional code would be extensive.

The code used [5] is based on a probability approach [6]. The chance P_i of a particle with the mean velocity $\overline{v}$ hitting a specific area A_i in a volume element V_s per unit time is given by

$$P_i = \frac{A_i}{V_s} \cdot \frac{\overline{v}}{4}. \qquad (1)$$

The surface elements A_i can be either warm or cold surfaces or openings to neighboring volume elements. This scalar approximation is an alternative to a time-consuming 3-dimensional treatment of the problem, if P_i is not strongly influenced by the spatial arrangement of the surfaces as is the case for volume elements with nearly cubic or spherical shapes. Very long tubes for example have to be subdivided into a series of short elements, the length of which is of the order of the diameter. This concept, however, leads to an excessive number of volume elements for tubes with a small ratio of diameter to length. Therefore, very long tubes are simulated in the code by two volume elements, which are connected by a small opening, the area of which is adjusted in such a way that the conductance of the long tube is reproduced. To get reliable results, the simplified MAFF beamline, as described above, is split into about 60 volume elements. Most of the simplifications mentioned previously have only a marginal effect on the code introduced in this section, since this code is only concerned with surface areas.

In addition to the probabilities P_i for the passage of the atoms through the vacuum system, probabilities for creation and diffusion in the source as well as for radioactive decay of the atoms were added to the Monte Carlo code. The probabilities for the creation are taken from data measured by Rudstam *et al.* [7] and calculations by Wahl [8]. Diffusion times are taken from ref. [7] tabulated half-lives and decay data are taken from ref. [9]. Measured release data are available form Zn to Sr and Pd to Ba. The elements Ni and Cu have been observed at ISOLDE and OSIRIS, but no release data have been published. All other elements have not been observed and no release data are known. Surface ionization probabilities have been calculated with the Langmuir equation [10] on a rhenium surface at 2700 K.

In a first step, the functionality of this code was verified by comparison to the MOVAK3D results for stable ions (N_2). The results are compared in table 2. Set 1 and Set 2 stand for two different sectoring approaches for the same geometry. The two sets differ in size and number of sectors used to describe the system. Set 2 is using more, but smaller sectors, which results in a higher agreement with the MOVAK3D simulation but also required a much longer calculation time.

From the relative values for Set 1, it is obvious, that the B-side pumps collect far too few atoms. This is due to an underestimation of the gap width between source trolley and beam tube by a factor of 10. The problem has been fixed in Set 2. This example gives an idea about the influence of the geometry.

The ratios S1/M and S2/M compare the different sectoring sets to the MOVAK3D simulation. Ignoring the last

Table 2. Comparison of the absorbed fraction of particles from MOVAK3D (M) and the scalar code. Set 1 (S1) and Set 2 (S2) represent two different sectoring approaches for the same geometry. See text for details.

	M	S1	S1/M	S2	S2/M
A_{total}	0.4019	0.5818	1.4	0.4826	1.2
A_{panel}	0.4018	0.5817	1.4	0.4826	1.2
A_{pumps}	$2 \cdot 10^{-4}$	$5 \cdot 10^{-5}$	0.3	$7 \cdot 10^{-5}$	0.4
B_{total}	0.5981	0.4182	0.7	0.5174	0.9
B_{panel}	0.5980	0.4182	0.7	0.5172	0.9
B_{pumps}	$2 \cdot 10^{-4}$	$9 \cdot 10^{-6}$	0.05	$3 \cdot 10^{-4}$	1.7

value, the average deviation for Set 1 is 50% and 30% for Set 2. The influence of sectoring within the same geometry is therefore in the order of 20%. The two programs agree within a factor of 2. A fixed version of the faster Set 1, with correct gap width, has been used to obtain the simulation results.

With confidence in the obtained results the calculation was extended to unstable nuclei.

Noble gases Xe and Kr, as well as the halogens I and Br are assumed volatile and stick only to cold surfaces. All other elements will stick to any surface they encounter until they decay to something volatile. The time of decay, surface and isotope type are collected in a 3-dimensional matrix. The time scale in this matrix is typically binned in steps of 1 day for a 10 year simulation or 3 days for 30 years of simulated time. From this matrix the activity of every element on every surface at any time can be determined.

The isotope specific activity information has also been used for shielding calculations, which are part of the code. A spherical symmetry is assumed for the shielding material and a 3-dimensional Monte Carlo method is used to calculate the absorption of radiation in the shielding material. Cross-sections for the photo-effect have been taken from ref. [11], for Compton scattering and electron-positron pair production formulas from ref. [12] have been used. Multiple Compton scattering and pair annihilation are included as well. To calculate the dose rate γ-ray energies and branching ratios are required additionally to the activity for each nuclide. The level schemes for short-lived isotopes with a few seconds half-life or less are especially complicated but unimportant for the shielding calculations. They only play a major role during the reactor cycle and a few minutes afterwards. Since the surroundings of MAFF will be inaccessible during this time for other reasons, there is no need to implement these nuclides. However, this alters the dose rate calculation for the slit system as shown in fig. 5. If the short-lived nuclides would be taken into account the dose rate would start and stay constant at a higher level. After turning off the reactor it would also drop down more rapidly. The calculation is accurate once the longer-lived isotopes start to dominate after 2 days. The dose rate has been calculated for energy absorption in water at 1 m distance.
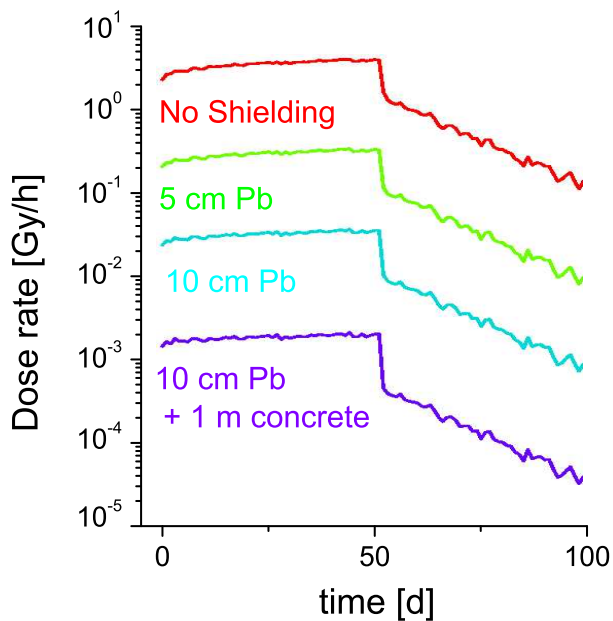
Fig. 5. Dose rate calculation at the MAFF slit system at 1 m distance. Isotope specific activity information is used as input for a three-dimensional Monte Carlo code. Photo absorption, Compton scattering, multiple Compton scattering and pair annihilation are included.

Fig. 6. Ion yield at the slit system. Best values of surface and laser ionization have been used. Measured release probabilities for fission fragments from a graphite matrix have been implemented. Ni and Cu have been observed at ISOL facilities but no release data have been published.

As a by-product of the simulation, the isotope yields at the mass pre-separator can be obtained, which is simply the amount of isotopes deposited on the slit system per second. For the yields shown in fig. 6 the best values of surface and laser ionization [13] have been used. Some isotopes of interest have very low yields due to low production, ionization and diffusion probabilities, resulting in statistically not significant numbers. Therefore, the yield is determined in a slightly different way. Low fission probabilities have been scaled up and ionization probabilities are set to 100% at first, so that all isotopes make it to the slit system. Afterwards, those probabilities have been multiplied by the true production and ionization probabilities and the correct yield is obtained.

2.3 Analytical calculations

The evolution of a radionuclide mixture is described theoretically by the radioactive decay law. The decay law for successive transformations [14] can be used to reproduce mother-daughter relations up to arbitrary order. For the purpose of this work, 9th order is sufficient.

For the analytical calculations all fission isotopes and isomeres from ^{65}Mn to ^{156}Eu have been taken into consideration. Multiplied by the production yields according to the Wahl Z_p model [8] and the fission rate, the in-source production yield can be obtained. Diffusion of elements out of the source is described by diffusion probabilities measured by Rudstam [7]. Ionization probabilities are calculated with the Langmuir equation [10].

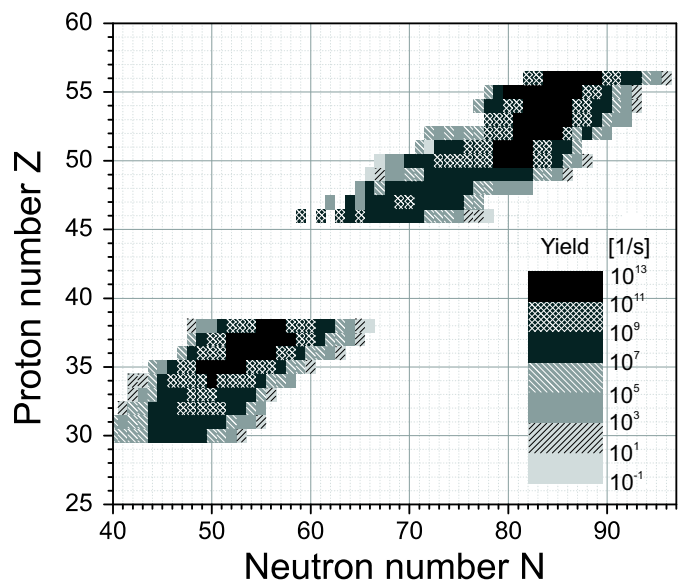Those isotopes, which manage to diffuse out off the ion source and get ionized, form the ion beam. Those that only

diffuse out off the ion source are not considered any further, while the remaining nuclides decay in the ion source until they form a stable isotope. However, at each intermediate element formed during the decay, there is a certain probability for ionization in which case the ion is counted as a part of the ion beam as well.

Finally, activities and dose rates (using a dose rate constant) are calculated from the remaining inventory. By default a dose rate constant for 2 MeV γ-ray energies has been used.

3 Distribution of atoms

3.1 Neutral isotopes

The non-volatile fission products, which leave the source with a kinetic energy corresponding to the source temperature of 2700 K, will cool down quickly due to wall interactions and finally stick to the wall in the vicinity of the ion source. If they decay to one of the four volatile elements (Xe, Kr, I, Br) they will start spreading again until they are trapped on one of the cryosurfaces, where they might decay to non-volatile elements. During the regeneration of these cryosurfaces, between reactor cycles, only the volatile elements will be released. In case of cryopanel regeneration, which is planned to be performed 3 days after the end of each reactor cycle, the radioactivity is transported to the nearest cryopump, an effect that can be seen in fig. 7. During the reactor cycle of 52 days, Xe is collected on the cryopanels until they are regenerated three days after the reactor shutdown and most of the atoms are transferred to the cryopump C3 on the B-side. This pump is now collecting the dominant part of the activity,
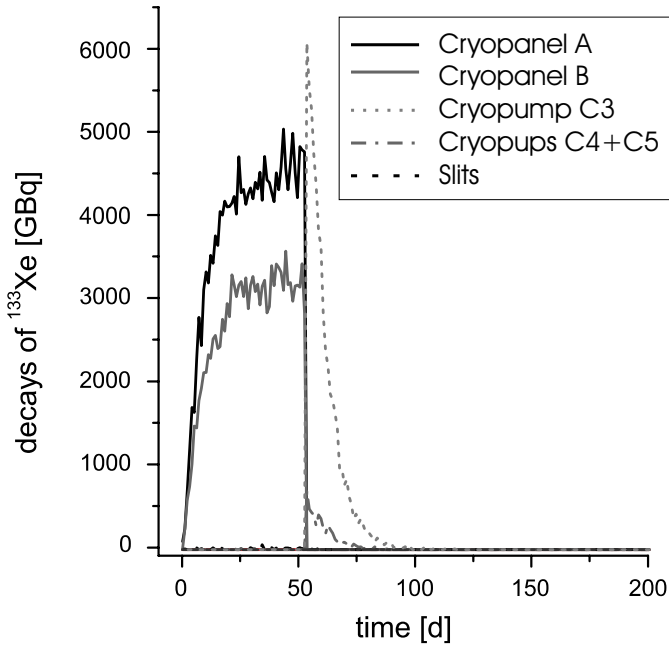
Fig. 7. Distribution of ^{133}Xe along the beam line. As a volatile nuclide Xe sticks only to cold surfaces. After 55 days the source trolley is removed and the cryopanels regenerated, resulting in the majority of the activity being gathered on the cryopump C3.

Table 3. Activity from Kr isotopes at the end of a reactor cycle (after 52 d) A_{52d}, 2.5 d later $A_{+2.5d}$ and 150 d later A_{+150d} under the assumption that no new activity is added.

Isotope	$T_{1/2}$	A_{52d} [Bq]	$A_{+2.5d}$ [Bq]	A_{+150d} [Bq]
^{83m}Kr	1.83 h	$5.3 \cdot 10^{11}$	0	0
^{85m}Kr	4.48 h	$1.3 \cdot 10^{12}$	$1.2 \cdot 10^{8}$	0
^{85}Kr	10.76 y	$2.6 \cdot 10^{9}$	$2.6 \cdot 10^{9}$	$2.5 \cdot 10^{9}$
^{87}Kr	76.3 min	$2.6 \cdot 10^{12}$	$1.6 \cdot 10^{-2}$	0
^{88}Kr	2.84 h	$3.4 \cdot 10^{12}$	$1.5 \cdot 10^{6}$	0
^{89}Kr	3.18 min	$4.4 \cdot 10^{12}$	0	0
^{90}Kr	32.3 s	$4.6 \cdot 10^{12}$	0	0
Kr total		$1.7 \cdot 10^{13}$	$1.2 \cdot 10^{8}$	$2.5 \cdot 10^{9}$

Table 4. Same as table 3 for Br isotopes.

Isotope	$T_{1/2}$	A_{52d} [Bq]	$A_{+2.5d}$ [Bq]	A_{+150d} [Bq]
^{83}Br	2.4 h	$5.4 \cdot 10^{11}$	$1.6 \cdot 10^{4}$	0
^{84f}Br	6 min	$9.6 \cdot 10^{11}$	$8.9 \cdot 10^{-23}$	0
^{85}Br	2.87 min	$1.3 \cdot 10^{12}$	0	0
^{86}Br	55.1 s	$1.8 \cdot 10^{12}$	0	0
^{88}Br	16.3 s	$1.9 \cdot 10^{12}$	0	0
Br total		$6.5 \cdot 10^{12}$	$1.6 \cdot 10^{4}$	0

Table 5. Same as table 3 for I isotopes.

Isotope	$T_{1/2}$	A_{52d} [Bq]	$A_{+2.5d}$ [Bq]	A_{+150d} [Bq]
^{129}I	$1.6 \cdot 10^{7}$ y	$3.6 \cdot 10^{3}$	$3.6 \cdot 10^{3}$	$4.1 \cdot 10^{3}$
^{131}I	8.02 d	$2.8 \cdot 10^{12}$	$2.3 \cdot 10^{12}$	$6.8 \cdot 10^{6}$
^{132}I	2.3 h	$4.3 \cdot 10^{12}$	$2.5 \cdot 10^{12}$	$6.0 \cdot 10^{-2}$
^{132m}I	83.6 min	$2.7 \cdot 10^{10}$	$2.9 \cdot 10^{-3}$	0
^{133}I	20.8 h	$6.6 \cdot 10^{12}$	$9.2 \cdot 10^{11}$	0
^{133}I	9 s	$1.7 \cdot 10^{11}$	0	0
^{134}I	52 min	$7.6 \cdot 10^{12}$	$7.9 \cdot 10^{-8}$	0
^{134m}I	3.5 min	$5.7 \cdot 10^{11}$	0	0
^{135}I	6.61 h	$6.0 \cdot 10^{12}$	$1.1 \cdot 10^{10}$	0
^{136}I	84 s	$2.8 \cdot 10^{12}$	0	0
^{136m}I	45 s	$1.7 \cdot 10^{12}$	0	0
I total		$3.2 \cdot 10^{13}$	$5.8 \cdot 10^{12}$	$6.8 \cdot 10^{6}$

Table 6. Same as table 3 for Xe isotopes.

Isotope	$T_{1/2}$	A_{52d} [Bq]	$A_{+2.5d}$ [Bq]	A_{+150d} [Bq]
^{129m}Xe	8.89 d	$9.3 \cdot 10^{3}$	$7.5 \cdot 10^{3}$	$2.1 \cdot 10^{-2}$
^{131m}Xe	11.9 d	$2.0 \cdot 10^{10}$	$2.0 \cdot 10^{10}$	$1.1 \cdot 10^{7}$
^{133}Xe	5.25 d	$6.6 \cdot 10^{12}$	$5.5 \cdot 10^{12}$	$2.0 \cdot 10^{4}$
^{133m}Xe	2.19 d	$2.0 \cdot 10^{11}$	$1.3 \cdot 10^{11}$	$7.6 \cdot 10^{-10}$
^{135}Xe	9.1 h	$8.0 \cdot 10^{11}$	$1.4 \cdot 10^{11}$	0
^{135m}Xe	15.3 min	$1.3 \cdot 10^{12}$	$1.8 \cdot 10^{9}$	0
^{137}Xe	3.83 min	$5.9 \cdot 10^{12}$	0	0
^{138}Xe	14.1 min	$5.9 \cdot 10^{12}$	0	0
Xe total		$2.1 \cdot 10^{13}$	$5.8 \cdot 10^{12}$	$1.1 \cdot 10^{7}$

since the source trolley is removed at this time and thus the beam tube offers a high conductance in this direction.

Once the cryopanels are regenerated and the activity has been collected in the pumps, the corresponding gate valves are closed and the cryopumps are regenerated. The radioactivity is transported by the roughing pumps towards a decay tank. The roughing pumps are dry, meaning they do not introduce any hydro-carbon contamination into the vacuum volume. There are two decay tanks on each side. Each tank will be filled over 3 reactor periods, while the material in the other tank is given 3 periods (> 150 d) time to decay.

Since only the four volatile elements Xe, Kr, I, and Br are released from the cryopump or -panel, only those elements will be found in the decay tanks. Also, only those fission products are transported into the tanks, and might be released from the vacuum system due to an air leak in case of a system failure. Tables 3 to 6 list all relevant isotopes of these elements and the corresponding activities at the end of a reactor cycle (52 d) as well as 2.5 days and 150 days after the end of the cycle assuming that no new activity is produced in the meantime.

These numbers should be compared to the yearly legal limits for the activity release of the FRM II as summarized in table 7. The daily limit is 1% of the year-round total. Comparing the inventory of Kr and Xe with the critical value, it can be seen that there is no danger to exceed the legal limits with Kr isotopes. After 2.5 days, when

Table 7. Legal emission limits for various radionuclides for the FRM II.

Agent	Yearly limit [Bq]
Noble gases	$2 \cdot 10^{13}$
Aerosols ($T_{1/2} \geq 8$ d)	$2 \cdot 10^{6}$
^{131}I	$1.8 \cdot 10^{8}$
^{14}C	$2 \cdot 10^{10}$
^{3}H	$3 \cdot 10^{12}$

the cryopanels are regenerated, the inventory is already well below the daily limit. For Xe the situation is less relaxed. During the regeneration of the panels the inventory is above the yearly limit. However, after 150 d decay the activity drops well below the limit and a release at this time is harmless.

For the halogens the situation is comparable. There is no long-living Br isotope which leads to no remarkable radioactive inventory after 150 days. Iodine has two long-living isotopes, ^{129}I and ^{131}I. Only the latter is responsible for noteworthy amounts of activity. At the end of a reactor cycle the inventory is above the limit but it decays rapidly within 150 days leaving only amounts that can be released safely.

Overall, it can be stated that the activities caused by decay of Xe, Kr, I, and Br do not cause any concerns. However, there might be problematic decay products, which will be discussed hereafter. According to calculation with the Z_p *model* after A. Wahl [8], the most abundant Xe isotopes are ^{135}Xe to ^{142}Xe, which are discussed below.

- ^{135}Xe decays to ^{135}Cs with a very long half-life of $2 \cdot 10^6$ y. Fortunately, it decays with β-radiation only.
- ^{136}Xe is stable.
- ^{137}Xe is short lived and decays to the long-lived nuclide ^{137}Cs ($T_{1/2} = 30.17$ y). During the 2.5 days between the end of the reactor cycle and the regeneration of the cryopanels ^{137}Xe will completely decay. At this time the total activity originating from ^{137}Cs is $2 \cdot 10^{10}$ Bq. The majority of the produced ^{137}Cs (99.98%) will remain on the cryopanels. The rest (0.02%) will be distributed among the various cryopumps, none of the Cs will reach the decay tanks.
- ^{138}Xe (14.1 min) and its daughter ^{138}Cs (32.2 min) are short lived and decay to stable Ba.
- ^{139}Xe (39.7 s), its daughter ^{139}Cs (9.3 min) and grand-daughter ^{139}Ba (83.06 min) are short lived and decay to stable La, before cryopanels or pumps are regenerated.
- ^{140}Xe (13.6 s) and its daughter ^{140}Cs (63.7 s) are short lived and decay to ^{140}Ba (12.75 d) and ^{140}La (40.3 h). After 2.5 days the total activity from one reactor cycle is $5 \cdot 10^{12}$ Bq for Ba as well as for La. This distributes along the beam-line according to table 1. Because of the half-life, there will be no significant buildup of activity caused by this isotopes. None of the mentioned Ba or La isotopes will reach the decay tanks.

- ^{141}Xe (1.7 s) decays via short-lived daughters (^{141}Cs (25 s), ^{141}Ba (18.3 min), ^{141}La (3.93 h)) to ^{141}Ce (32.5 d), which has a half-life in the order of one reactor cycle. The total ^{141}Ce activity produced during one reactor cycle, and 2.5 days decay time, is $4 \cdot 10^{12}$ Bq distributed along the beam-line according to table 1. ^{141}Ce decays to stable ^{141}Pr. None of the ^{141}Ce atoms will reach the decay tanks.
- ^{142}Xe (1.24 s) decays via short-lived daughters (^{142}Cs (1.7 s), ^{142}Ba (10.7 min), ^{142}La (92.5 min)) to stable ^{142}Ce.

The less abundant isotopes with $A > 142$ are produced with individual yields $Y < 5 \cdot 10^{-4}$ atoms/fission. Since all daughters of Xe are non-volatile, they will only leave the ion source as atoms unless they are produced by decay from Xe outside the source. With the decreasing individual yield for heavy Xe isotopes the chance of finding its daughters outside the source decreases. The activity caused by these isotopes can be neglected in comparison with other sources of radiation.

Iodine decays to xenon, which has been discussed above.

The noble gas krypton is produced with individual yields $Y > 1 \cdot 10^{-4}$ atoms/fission for $A < 95$. The resulting decay chains are discussed below.

- ^{85}Kr is long lived (10.76 y) and decays to stable ^{85}Rb. It will eventually be regenerated in the decay tanks where it will build up to activities $< 8 \cdot 10^9$ Bq.
- ^{86}Kr is stable.
- ^{87}Kr decays to ^{87}Rb ($4.8 \cdot 10^{10}$ y), which decays without γ-emission.
- ^{88}Kr decays via ^{88}Rb (17.8 min) to stable ^{88}Sr.
- ^{89}Kr decays via ^{89}Rb (15.2 min) to long-lived ^{89}Sr (50.5 d). ^{89}Sr favors β-decay to ^{89}Y ground state. The branching ratio to ^{89m}Y (16 s) is only $9.6 \cdot 10^{-5}$. The resulting γ activity is in the MBq range. ^{89m}Y will distribute along the beam-line as shown in table 1, but will not reach the decay tanks.
- ^{90}Kr decays via ^{90}Rb (4.3 min) to ^{90}Sr (28.6 y). The latter decays without γ-radiation to ^{90}Y (64.1 h). Populated by ^{90}Sr, the activity of ^{90}Y saturates at $2 \cdot 10^{10}$ Bq. ^{90}Y favors β-decay to ^{90}Zr ground state (99.9885%). It will distribute along the beam-line as shown in table 1, but will not reach the decay tanks.
- ^{91}Kr decays via ^{91}Rb (58 s) and ^{91}Sr (9.5 h) to ^{91}Y (58.5 d). ^{91}Y favors β-decay to ^{91}Zr ground state. The branching ratio to ^{91m}Zr (0.17 ps) is only $3 \cdot 10^{-3}$. The resulting γ activity is in the GBq range. ^{91m}Zr will distribute along the beam-line as shown in table 1, but will not reach the decay tanks.
- ^{92}Kr decays via short-lived daughters (^{92}Rb (4.5 s), ^{92}Sr (2.71 h), ^{92}Y (3.54 h)) to stable ^{92}Zr.
- ^{93}Kr decays via short-lived daughters (^{93}Rb (5.8 s), ^{93}Sr (7.45 min), ^{93}Y (10.1 h)) to long-lived ^{93}Zr ($1.5 \cdot 10^6$ y). ^{93}Zr decays by β-emission with a branching ratio of 95% to ^{93m}Nb (16.13 y). It emits very soft 31 keV γ-radiation to the stable ground state. It will distribute along the beam-line as shown in table 1, but will not reach the decay tanks.

Table 8. List of volatile compounds of Sr, Y, Zr, Nb, Sb, and Te, their melting point T_m, boiling point T_B and decomposition point T_D.

Element or compound	T_m [K]	T_B [K]	T_D [K]
Sr	1050	1655	
SrH$_2$			1323
SrO	2803/2938	3273	
SrO$_2$	solid		488
Sr$_3$N$_2$	solid		
Y	1799	3609	
Y$_2$O$_3$		704	
YO			
YO$_2$			
Zr	2128	4682	
ZrO$_2$	2950/2983		
ZrN	3233		
Nb	2750	5017	
NbO	2210		
NbO$_2$	2173		
Nb$_2$O$_5$	1733/1758		
NbN	2573		
Sb	903	1860	
SbO			
SbO$_2$			
SbH$_3$	185	256	
Sb$_2$O$_3$	928	1518	
Sb$_2$O$_4$	solid		
Sb$_2$O$_5$	solid		653
Te	723	1261	
TeO			
TeO$_2$	1006	1518	
TeO$_3$	973	1703	

Table 9. Same as table 8 for I, Cs, Ba, Ce, and Pr.

Element or compound	T_m [K]	T_B [K]	T_D [K]
I	387	457	
IO$_2$			
IO$_3$			
I$_2$O$_4$	solid		403
I$_2$O$_5$	solid		573
I$_4$O$_9$			348
Cs	302	944	
CsH	solid		443
CsO$_2$	873/705		
Cs$_2$O	763		
Cs$_2$O$_2$	863		
Ba	1000	2143	
BaH$_2$	solid		1473/948
BaO	2246/2186	2273	
BaO$_2$	solid		723
Ba$_3$N$_2$	solid		1273
Ce	1068	3633	
CeH$_2$ (s)			
CeO$_2$	2673		
Ce$_2$O$_3$	2503		
CeN	2830		
Pr	1208	3563	
PrO$_2$	solid		623
Pr$_2$O$_3$	2573		

tanks can be observed with γ spectroscopy and serve as an indicator for the radioactive fill level of the tank.

3.2 Volatile compounds

Besides the volatile elements, there is the possibility of forming volatile compounds, *e.g.* oxides. A list of known compounds is given in table 8 and continued in table 9 [15]. It is highly unlikely that these compounds can be formed under vacuum condition. However, their formation might be possible in case of air intake into the system. Since the amount of fission fragments is very small, it is highly unlikely that compounds, with more than one fission fragment, are formed. Melting points are listed for reasons of completeness. However, the concept of melting can hardly be applied to individual fission fragments. Compounds for which only a melting point is listed in table 8 disintegrate before they evaporate. Compounds with only a decomposition point listed disintegrate before melting. Compounds without boiling, melting or decomposition temperature have been observed but no data are available. Boiling temperatures serve as an indicator for the vapor pressures.

– ^{94}Kr decays via short-lived daughters (^{94}Rb (2.7 s), ^{94}Sr (74 s), ^{94}Y (18.7 min)) to stable ^{94}Zr.

Bromide decays to krypton which has been studied above.

For the volatile elements one can conclude that they do not pose a danger to the environment or people as long as the described operation procedures are enforced. It must be added, however, that elemental Br and I are chemically very active substances and it is very unlikely to find them unbound. It is even doubtful that they are volatile at all. Nevertheless, this was assumed throughout all calculations for the sake of conservatism. It has been shown that the decay products ^{90}Y, ^{91m}Zr, ^{137}Cs, ^{140}Ba, ^{140}La, and ^{141}Ce lead to noteworthy amounts of γ-radiation sources on the cryopumps. The most dominating γ-radiation source that will reach the decay tanks is ^{85}Kr. Its activity in the decay

Table 10. Same as table 3 for Te isotopes.

Isotope	$T_{1/2}$	A_{52d} [Bq]	$A_{+2.5d}$ [Bq]	A_{+150d} [Bq]
^{127m}Te	109 d	$7.4 \cdot 10^6$	$7.3 \cdot 10^6$	$2.8 \cdot 10^6$
^{127}Te	9.35 h	$1.2 \cdot 10^{11}$	$8.3 \cdot 10^{10}$	$2.7 \cdot 10^6$
^{129m}Te	33.6 d	$8.7 \cdot 10^{10}$	$8.4 \cdot 10^{10}$	$4.0 \cdot 10^9$
^{129}Te	69.6 min	$5.8 \cdot 10^{11}$	$5.4 \cdot 10^{10}$	$2.6 \cdot 10^9$
^{131m}Te	30 h	$3.1 \cdot 10^{11}$	$7.8 \cdot 10^{10}$	0
^{131}Te	25 min	$2.6 \cdot 10^{12}$	$1.7 \cdot 10^{10}$	0
^{132}Te	76.3 h	$4.2 \cdot 10^{12}$	$2.5 \cdot 10^{12}$	$5.8 \cdot 10^{-2}$
Te total		$7.8 \cdot 10^{12}$	$2.5 \cdot 10^{12}$	$6.6 \cdot 10^9$

Compounds with high boiling points, have a very low vapor pressure, and thus cannot be considered volatile. With these constraints in mind only the compounds of iodine and tellurium remain as possible candidates for volatile compounds. Iodine has already been discussed. A summary of longer-lived tellurium isotopes is given in table 10. The Te activity is comparable to the Kr activity, which is below the legal limits.

3.3 Aerosols

The third way to create volatile activity from non-volatile radionuclides are aerosols. Aerosol is a very general term applied to all suspensions of solid or liquid particles in a gas, *e.g.* air. Typical aerosol dimensions reach from 1 nm to 100 μm, with the average diameter being 0.1 μm. The limit set by the European Commission [16,17] for average aerosol content, smaller than 10 μm, is 50 μg/m^3.

To calculate the actual number of aerosols per cubic meter, it is necessary to estimate their density. Since the ion source is graphite loaded it seems reasonable to use the density of carbon. Doing so, the amount of aerosols can be calculated for different radii. At 1 nm radius $5 \cdot 10^{18}$ aerosols can be calculated. This number reduces with the third power of the radius.

Under vacuum conditions the gas can sustain less aerosols compared to ambient pressure. To reflect this a simple linear dependence is assumed. MAFF will be operated at a pressure of $1 \cdot 10^{-6}$ h Pa. This is nine orders of magnitude below ambient pressure. It is assumed that the amount of aerosols sustained under vacuum is reduced by the same amount.

An aerosol by itself, however, is not radioactive. To form a radioactive aerosol, a radionuclide must bind to an aerosol particle. A list of radionuclides, which must be taken into account for aerosol formation, is given in tables 11 and 12 for refractory elements, which will stay in the ion source even at 2700 K, and volatile elements, respectively. The nobel gases have not been taken into account here, since they form no compounds.

The probability of a radionuclide clustering to an aerosol is very small. Using geometrical cross-section considerations a mean free path of over 40 m can be calculated for a radionuclide before it collides with a residual gas

Table 11. Refractory fission fragments with half-life of 8 days or more are potential candidates for formation of dangerous aerosols. N_{52d} is the inventory after a reactor cycle of 52 d. See table 3 for additional explanation of columns.

Isotope	$T_{1/2}$ [d]	N_{52d}	A_{52d} [Bq]	A_{+150d} [Bq]
^{91}Y	58.5	$2.0 \cdot 10^{19}$	$2.7 \cdot 10^{12}$	$4.6 \cdot 10^{11}$
^{93}Zr	$5.48 \cdot 10^8$	$2.8 \cdot 10^{19}$	$4.0 \cdot 10^5$	$4.0 \cdot 10^5$
^{95}Zr	64	$2.2 \cdot 10^{19}$	$2.8 \cdot 10^{12}$	$5.5 \cdot 10^{11}$
^{95}Nb	35	$4.9 \cdot 10^{18}$	$1.1 \cdot 10^{12}$	$9.5 \cdot 10^{11}$
^{99}Tc	$7.67 \cdot 10^7$	$2.5 \cdot 10^{19}$	$2.6 \cdot 10^6$	$2.8 \cdot 10^6$
^{103}Ru	39.35	$8.8 \cdot 10^{18}$	$1.8 \cdot 10^{12}$	$1.3 \cdot 10^{11}$
^{106}Ru	373.6	$1.7 \cdot 10^{18}$	$3.7 \cdot 10^{10}$	$2.8 \cdot 10^{10}$
^{125}Sb	985.5	$1.2 \cdot 10^{17}$	$9.4 \cdot 10^8$	$8.4 \cdot 10^8$
^{126}Sb	12.4	$2.7 \cdot 10^{14}$	$1.7 \cdot 10^8$	$8.3 \cdot 10^4$
^{141}Ce	33	$1.5 \cdot 10^{19}$	$3.8 \cdot 10^{12}$	$1.6 \cdot 10^{11}$
^{144}Ce	284	$2.3 \cdot 10^{19}$	$6.4 \cdot 10^{11}$	$4.5 \cdot 10^{11}$
^{143}Pr	13.6	$9.1 \cdot 10^{18}$	$5.4 \cdot 10^{12}$	$2.9 \cdot 10^9$
^{147}Nd	10.98	$2.9 \cdot 10^{18}$	$2.1 \cdot 10^{12}$	$1.6 \cdot 10^8$
^{147}Pm	956.3	$6.7 \cdot 10^{18}$	$5.7 \cdot 10^{10}$	$7.3 \cdot 10^{10}$
^{151}Sm	33945	$4.5 \cdot 10^{17}$	$1.1 \cdot 10^8$	$1.3 \cdot 10^8$
Total		$1.7 \cdot 10^{20}$	$2.0 \cdot 10^{13}$	$2.8 \cdot 10^{12}$

Table 12. Same as table 11 for volatile aerosol candidates.

Isotope	$T_{1/2}$ [d]	N_{52d}	A_{52d} [Bq]	A_{+150d} [Bq]
^{89}Sr	50.5	$1.5 \cdot 10^{19}$	$2.4 \cdot 10^{12}$	$3.1 \cdot 10^{11}$
^{90}Sr	10585	$2.6 \cdot 10^{19}$	$2.0 \cdot 10^{10}$	$2.0 \cdot 10^{10}$
^{126}Sn	$8.56 \cdot 10^7$	$2.0 \cdot 10^{17}$	$4.3 \cdot 10^4$	$4.3 \cdot 10^4$
^{127}Te	109	$5.6 \cdot 10^{15}$	$1.2 \cdot 10^{11}$	$2.8 \cdot 10^6$
^{129}Te	33.5	$3.7 \cdot 10^{17}$	$8.7 \cdot 10^{10}$	$4.0 \cdot 10^9$
^{129}I	$6.21 \cdot 10^9$	$2.6 \cdot 10^{18}$	$3.6 \cdot 10^3$	$4.1 \cdot 10^3$
^{131}I	8	$2.8 \cdot 10^{18}$	$2.8 \cdot 10^{12}$	$6.8 \cdot 10^6$
^{135}Cs	$1.10 \cdot 10^9$	$3.6 \cdot 10^{18}$	$3.4 \cdot 10^4$	$3.7 \cdot 10^4$
^{137}Cs	10950	$2.7 \cdot 10^{19}$	$2.0 \cdot 10^{10}$	$2.0 \cdot 10^{10}$
^{140}Ba	13	$9.1 \cdot 10^{18}$	$5.7 \cdot 10^{12}$	$1.7 \cdot 10^9$
Total		$8.7 \cdot 10^{19}$	$1.1 \cdot 10^{13}$	$3.6 \cdot 10^{11}$

atom at vacuum pressure. Aerosol-radionuclide collisions are obviously very rare.

For conservativeness sake, it is assumed that aerosols can somehow manage to acquire a complete monolayer of radionuclides on their surface. The amount of radionuclides that can cluster to an aerosol can be derived by simple geometric considerations, assuming both partners to be spherical. Since there are always unfilled volumes between spheres an additional correction factor must be added, assuming closest packing.

Combining all of the above, but the cluster probability, the maximum activity sustainable by aerosols per m^3 can be derived. The obtained activities have been normalized by the yearly allowance of $2 \cdot 10^6$ Bq, and plotted in fig. 8.
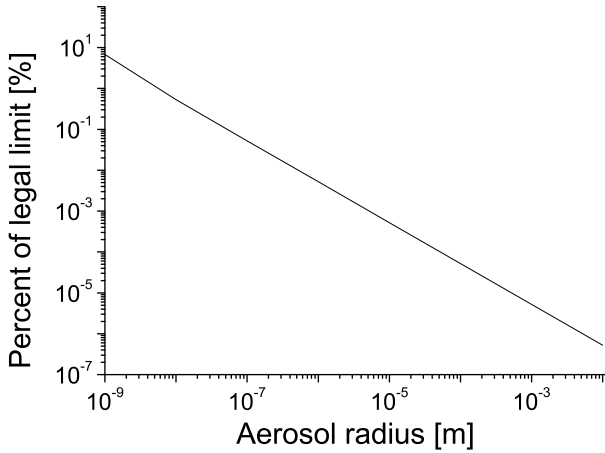
Fig. 8. Expected aerosol activity compared to the legal limit for different aerosol diameters.

It can be seen from fig. 8, that even for the smallest aerosol diameters the activity from aerosols, immediately after the end of a reactor cycle, is small compared to the threshold. Additional safety margins arise from the facts that typical aerosols have $0.1\,\mu$m radius and not 1 nm (safety factor: $7.7 \cdot 10^{-3}$), that the reactor has an aerosol filter installed (10^{-5}) and the decay time of 150 d ($9.95\cdot10^{-2}$). Combining all three gives a final safety factor of $7.7 \cdot 10^{-9}$.

3.4 α activity

Special consideration is necessary for α activity coming from uranium and plutonium produced from ^{238}U by thermal neutron capture and β-decay. Both elements can be implanted in the slit system due to diffusion of uranium out of the graphite matrix, subsequent ionization and ion-beam transport. An uranium inventory of 1.2 g (99.9% enriched ^{235}U) corresponds to $3.1 \cdot 10^{21}$ uranium atoms. Because of the small amount of uranium in the matrix compared to carbon it is justified to assume the same release rate W for uranium as for graphite [18]:

$$W = 0.077 \cdot p\sqrt{\frac{M}{T}} \left[\frac{\mathrm{g}}{\mathrm{cm^2\,s}}\right]. \qquad (2)$$

This gives a release rate of $4.11 \cdot 10^{-7} \frac{\mathrm{g}}{\mathrm{cm^2\,s}}$ for mass number $A = 12$, temperature $T = 2400$ K and graphite vapor pressure $p = 7.5 \cdot 10^{-5}$ Pa. The relevant area is the 2 mm diameter hole in the rhenium cylinder of the ion source. Therefore the release rate is 0.057 g/50 d. The surface ionization probability of 0.162% for uranium is used for plutonium as well, for the purpose of this estimate. For 100 fissioned ^{235}U atoms, 16 are converted to ^{236}U by thermal neutron capture. Disregarding decay the isotope ratio at the slit system is calculated to the values shown in table 13.

Using the well-known half-lives and disregarding decay over 150 reactor cycles one finds rather low activity after one reactor period and even after 30 years of operation, as listed in table 14.

Table 13. Ratio of isotopes decaying by α-radiation at the slit system.

Percentage	Isotope
97.6%	^{235}U
2.3%	^{236}U
0.1%	^{238}U
$6.2 \cdot 10^{-5}$%	^{239}Pu
$1.9 \cdot 10^{-6}$%	^{240}Pu

Table 14. α activity on the slit system from uranium and plutonium released from the ion source as uranium.

Isotope	After 50 d	After 30 y
^{235}U	0.35 Bq	52 Bq
^{236}U	0.25 Bq	37 Bq
^{238}U	56 μBq	8.4 mBq
^{239}Pu	0.01 Bq	1.5 Bq
^{240}Pu	0.7 mBq	0.1 Bq

Even from this coarse estimate it can be seen, that α activity caused by uranium or plutonium is very small compared to β activity created by fission fragments. The contribution from plutonium is so low that 99% enriched ^{235}U would be sufficient.

3.5 Volume activity

Volume activity comes from volatile or non-volatile radionuclides travelling through the vacuum volume. A reasonably conservative estimate for this amount can be made by comparing the time an atom spends travelling to the total time a reactor cycle lasts. Most atoms travel some milliseconds. Therefore 1 s is a reasonable upper limit. Comparing 1 s to 52 days (4.5 Ms) gives a fraction of $2.2 \cdot 10^{-7}$ in the volume, which is comparably low.

A similar amount can be derived for the activity contained in the ion beam. At 30 keV beam energy, the average ion has a velocity of $2 \cdot 10^{5}$ m/s. At this speed ions spend only 5 μs in the beam tube. It is obvious that this contribution is small compared to the volume activity caused by radionuclides in the residual gas.

4 Distribution of ions

4.1 Contamination by the ion beam

If the ion beam collides with any material (*e.g.* slit system, ion optic elements, beam diagnostic elements, valves, beam dump, target) it will implant deeply the ions and contaminate the material. The potential activity transported by the beam on its way to the mass pre-separator is especially severe since the beam contains all ions produced by the source.

Table 15. Dose rates from ion beam in 1 m distance for average γ-decay energies of 2 MeV. See text for details.

Isotope	$T_{1/2}$ [d]	Dose [μSv/h]
^{140}La	1.68	$2.4 \cdot 10^5$
^{140}Ba	13	$2.3 \cdot 10^5$
^{89}Sr	50.5	$3.4 \cdot 10^3$
^{137}Cs	10950	$4.8 \cdot 10^2$
^{91}Y	58.5	$2.2 \cdot 10^2$
^{141}Ce	33	$1.6 \cdot 10^2$
^{90}Sr	10585	37
^{90}Y	2.67	31
^{143}Pr	13.6	6.5
^{86}Rb	19	2.7

Table 16. Dose rates from ion beam in 1 m distance for average γ-decay energies of 2 MeV. See text for details.

Mass	Dose [μSv/h]
140	$4.7 \cdot 10^5$
89	$3.4 \cdot 10^3$
137	$4.8 \cdot 10^2$
91	$2.2 \cdot 10^2$
141	$1.6 \cdot 10^2$
90	68
143	9.1
86	2.7
95	1.5
144	0.6

Table 17. Iodine with 30 keV beam energy is impinged on various target materials. Target density ρ and target surface binding energy B_s are given. The resulting sputter yield Y_s, the energy E_s of the sputtered atoms together with the range R and the lateral straggle S of incoming ions are noted.

Target	ρ [g/cm^3]	B_s [eV]	Y_s	E_s [eV]	R [Å]	S [Å]
Cu	8.92	3.52	11.4(2)	32.1(6)	82	33
Al	2.70	3.36	3.61(4)	44.6(4)	202	55
Ti	4.52	4.89	2.89(9)	69(2)	146	49
C	2.25	4.41	1.73(5)	40.1(12)	208	34
Fe	7.87	4.34	6.9(2)	41.3(12)	87	33
Pb	11.34	2.03	18.2(5)	91(3)	115	66

Table 15 shows the ten isotopes with the highest dose rates seven days after the end of a 52 d reactor cycle, calculated with the analytical approach described above. In table 16 the same top ten is given for the mass branches.

For the radioactivity distribution it is important to know weather or not activity implanted in the slit system or other *hot spots* will be released due to sputter effects. Without any modifications to the slit system, sputter yields as shown in table 17 are expected. This would result in a contamination of the adjacent magnet chamber, requiring additional shielding for the magnet as well. The effect of sputtering has been studied in simulations with SRIM2003 [19] and in test experiments using a 30 keV ion beam. Both approaches went hand in hand but will be introduced here in steps. For more detailed information, please consult refs. [5,20].

4.1.1 Theoretical considerations

In principle there are two ways to reduce the amount of atoms released from the slit system into the magnet chamber. The first approach is to use a geometry that reduces the amount of sputtered atoms released from the slit system. The simplest option is to introduce an aperture that reduces the solid angle available for sputtered atoms back out of the system, as shown in fig. 9a. Applying this geometry reduces the sputter yield into the magnet chamber (effective sputter yield) by 75%.

The effective sputter yield can be further reduced by taking the distribution of the sputtered atoms into account. The sputtered atoms follow some inflated cosine distribution favoring the zero-degree angles [21]. A possible distribution is indicated in fig. 9. Taking advantage of the cosine distribution a wedge-shaped target structure, as shown in fig. 9b, can reduce the effective sputter yield. A decrease by a factor of 10 seems possible for multiple small wedges. The use of multiple small wedges has the advantage of a steep angle of inclination and low height, while simultaneously covering a large base area. However, SRIM2003 simulation show, that the sputter yield increases with the angle of impact.

Taking the wedge idea to the limit leads to the use of razor blades as wedges with very small base. Two stacks of razor blades have been investigated. A stack of 12 blades separated by 0.5 mm has been used to further exploit the solid-angle reduction, while a stack of 50 blades with no space in between has been used as multiple very small wedges.

Alternatively, the effective sputter yield can be reduced by using a material which offers a very low intrinsic sputter
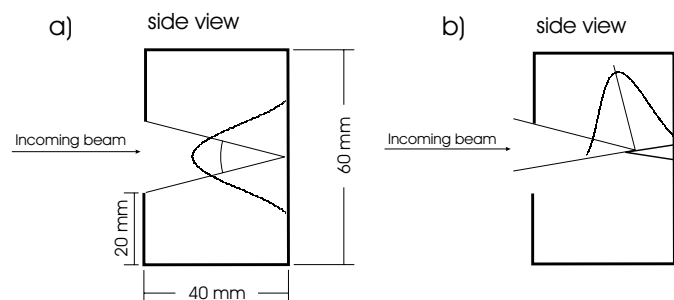
Fig. 9. Layout for a slit system aiming to reduce the sputter yield. By a) exploiting solid-angle reduction only, and by b) installing a wedge at the end of the box, taking advantage of the cosine distribution of sputtered atoms.

capability. The sputter properties of various materials, as listed in table 17, have been studied with SRIM2003.

It can be seen, that the sputter yield reduces with the material density and increasing surface binding energy. Both properties make carbon the ideal choice as a target. The dependence on the density has been studied for carbon and found to be linear. This suggests that a low density carbon target would be a good choice to reduce the sputter yield. The carbon target that was experimentally suited was the POCO carbon foam [22].

4.1.2 Experimental setup

Experiments have been performed at the ion source test stand of the MLL with a parallel, mass separated, 30 keV, negative iodine beam impinging on various targets encased in a box as shown in fig. 9. The box was set up as a Faraday cup to measure the on-target ion current. The opening slit was covered with a silicon waver (with a small hole in the center for the ion beam) as a catcher material for the sputtered atoms. The ion current was recorded and the silicon waver was analyzed later with Rutherford Backscattering (RBS) at Forschungszentrum Rossendorf (FZR).

4.1.3 Experimental results

At FZR, various data points on the silicon wavers have been scanned in x- and y-direction centered around the hole for the ion beam. From the measured data points a two-dimensional map describing the atom coating of the silicon waver has been created. Integrating the map gives the total number of sputtered atoms on the waver. From the integrated ion current the total number of incoming ions can be determined. The ratio of both values leads to the effective sputter yield, which is listed in table 18 with statistical errors for the various targets tested.

4.2 Ion gas collisions

Ions can collide with residual gas atoms, where charge exchange or scatter processes result in ion loss. Those lost ions will collide with walls eventually and contribute to the contamination of beam tube walls. SRIM2003 simulations for 30 keV ^{140}Ba ions passing through air under

Table 18. Summary of effective iodine sputter yields for all tested target materials.

Target	Iodine sputter yield
Flat	$1.09(3) \cdot 10^{-1}$
Wedges	$9.4(2) \cdot 10^{-2}$
12 blades	$9.2(3) \cdot 10^{-3}$
50 blades	$2.2(1) \cdot 10^{-2}$
POCO	$6.8(18) \cdot 10^{-4}$

various pressures have indicated that for an air pressure of 10^{-6} hPa the loss rate is 10^{-7} per meter.

At this loss rate, the contribution of the ion beam to contamination before the slit system will be $50 \, \mathrm{nSv \, h^{-1} \, m^{-1}}$. The dose rate is given for a decaying period of 7 d. During operation the level will be in the magnitude of $1 \, \mu\mathrm{Sv/h}$.

Behind the slit system the dose rates will be even lower, since only two mass branches will be transported to the experiments.

5 Summary

The impact of the distribution of radioactive fission fragments on contamination and radiation safety of a RIB facility has been studied using the example of the MAFF project. Gaseous elements (Br, Kr, I, and Xe), aerosols, and oxides have been taken into account as volatile elements. All produced volatile activities are within legal limits if a decay time of 150 d is used. Especially aerosols are expected to play only a minor role for radiation release.

Investigation of the radioactive ion beam inventory has shown that a high amount of contamination must be expected at *hot spots*, where a majority of the beam is lost. To reduce the contamination past the slit system it seems reasonable to omit at least mass 140 and 89 from passing this point.

The experimental search, first introduced in ref. [5], for a surface material with extremely low sputter yield has shown that low density carbon foam is an ideal material for slit system coating to avoid contamination of the adjacent magnet chamber.

In conclusion it can be found that activities at MAFF, even so a 1000 times larger compared to ISOLDE, can be handled equally safe under normal operation, if some additional safety features (*e.g.* croypumping, decay tanks, carbon-coated slit system) are installed.

References

1. T. Faestermann *et al.*, Nucl. Phys. A **746**, 22 (2004).
2. J. Matauch, R. Herzog, Z. Phys. **89** (11-12), 786 (1934).
3. G. Class, Movak3D, www.lv-soft.de (2004).
4. J. Szerypo, W. Assmann, M. Groß, D. Habs, O. Kester, P.G. Thirolf, F. Nebel, E. Zech, T. Faestermann, R. Krücken, P. Maier-Komor, Nucl. Instrum. Methods A **561**, 76 (2006).
5. F. Nebel, E. Zech, T. Faestermann, R. Krücken, P. Maier-Komor, W. Assmann, J. Szerypo, M. Groß, D. Habs, O. Kester, P.G. Thirolf, R. Grötzschel, Nucl. Instrum. Methods A **561**, 83 (2006).
6. R.A. Haefer, *Cyropumping* (Clarendon Press, Oxford, 1989).
7. G. Rudstam *et al.*, Radiochim. Acta **49**, 155 (1990).
8. A. Wahl, At. Data Nucl. Data Tables **39**, 1 (1988).

9. R. Firestone, V. Shirley (Editors), *Table of Isotopes*, 8th edition (John Wiley & Sons, New York, 1996).

10. U. Köster, *Yields and spectroscopy of radioactive isotopes at LOHENGRIN and ISOLDE*, PhD Thesis, TU München (2000).

11. K. Siegbahn, *Alpha-, Beta-, and Gamma Ray Spectroscopy* (North Holland, 1965).

12. P. Marmier, *Kernphysik* (Verlag des Vereins der Mathematiker und Physiker an der ETH Zürich, Zürich, 1968).

13. U. Köster, private communication.

14. K.H. Lieser, *Nuclear and Radiochemistry* (VCH, Weinheim, New York, 1997).

15. D.R. Lide (Editor), *CRC Handbook of Chemistry and Physics*, 82nd edition (CRC Press, Boca Raton, 2002).

16. European Commission, Directive 96/62/EC (1996).

17. European Commission, Directive 99/30/EC (1999).

18. P. Maier-Komor, *SPD Katalog* (Materials Research GmbH, München, 1981).

19. J.F. Ziegler, *SRIM - The stopping and range of ions in matter*, `www.srim.org` (2004).

20. F. Nebel, *Radionuclides at MAFF*, PhD Thesis, Technische Universität München (2006).

21. W. Eckstein, private communication.

22. J.W. Klett, *Process for making carbon foam*, US-patent: 6033506 (1997).